RSC Advances

PAPER

View Article Online
View Journal | View Issue

Cite this: *RSC Adv.*, 2019, **9**, 34677

Enhanced thermal conductivity and tensile strength of Al–17Si–3.5Cu with SiC-nanoparticle addition

D. P. Jiang * and J. K. Yu

The morphology and size of primary Si has a significant influence on the thermal conductivity (TC) and strength of Al–17Si–3.5Cu. In this study, the effect of a 1–3 wt% SiC nanoparticle (SiC_{nps}) addition on TC and tensile strength of Al–17Si–3.5Cu was investigated. Nanoparticles distributed at the interface between primary Si and Al led to a significant refinement of primary Si; for example, a primary Si size of 2 μm with 3 wt% SiC_{nps} addition was achieved. TC of SiC_{nps}/Al–17Si–3.5Cu improved with an increase in nanoparticle content. Nanoparticles distributed at the interface between Si and Al reduced the interfacial thermal resistance. Thus, the effective TC of eutectic Si increased. Owing to the refinement of the primary Si and the increased interfacial thermal resistance, originating from the high content of SiC_{nps} at the interface, the effective TC of primary Si decreased. Compared with Al–17Si–3.5Cu, contribution to the improvement of the TC of SiC_{nps}/Al–17Si–3.5Cu resulted mainly from eutectic Si. Due to the refinement of primary Si, the tensile strength of SiC_{nps}/Al–17Si–3.5Cu improved with an increase in SiC_{nps} content. When the SiC_{nps} content was 3 wt%, the yield strength, ultimate tensile strength and elongation of SiC_{nps}/Al–17Si–3.5Cu were ~176 MPa, 418 MPa and 7%, respectively, which were improved by 37.5%, 53.7% and 218%, respectively, when compared with Al–17Si–3.5Cu.

Received 10th September 2019
Accepted 22nd October 2019

DOI: 10.1039/c9ra07253e

rsc.li/rsc-advances

1. Introduction

Hypereutectic Al–Si alloys are used extensively in many fields, such as automobiles, electronic packaging and military applications, due to their low mass, high corrosion resistance, high thermal conductivity (TC) and outstanding mechanical performance.[1–4] In the vehicle field, as piston materials, hypereutectic Al–Si–Cu alloys are required to have a high TC and excellent mechanical properties. Primary Si, an important phase that consists of hypereutectic Al–Si–Cu alloys, exerts a significant influence on the properties of the alloy. Coarse and irregular primary Si deteriorates the mechanical properties and machinability of Al alloys. As a result, numerous efforts have been made to refine primary Si. The refinement of primary Si in hypereutectic Al–Si alloys can be achieved by various methods, such as Al–P, Al–Fe–P and the Al–Ti–P–C master alloy, rare element and ultrasonic treatment, and electromagnetic stirring.[5–14] Although primary Si can be refined by traditional processes, many methods are either complex and cannot be used on a large scale, or they reduce the TC of the Al–Si alloy considerably.

Recent investigations have shown that Al_2O_3 nanoparticles can refine the primary Si and eutectic Si in the local hypereutectic Al–Si–Cu alloy area simultaneously.[15] Compared with these traditional methods, nanoparticle addition can refine primary Si and activate the Orowan strengthening effect in hypereutectic Al–Si alloys. Al_2O_3 nanoparticles hinder the primary Si phase from growing by distributing on the Al/Si interface, thereby leading to the refinement of primary Si. It has also been illustrated that nanoparticles in hypoeutectic Al–Si alloys lead to the refinement of the eutectic Si phase, such as TiCN and AlN.[16,17] However, some investigations have focused on the effect of nanoparticles on the microstructures of hypereutectic Al–Si, inadequate studies exist on the effect of nanoparticles on the TC of hypereutectic Al–Si. Although nanoparticles have refined the microstructures of Al–Si, the effect of nanoparticles on the TC of the alloy remains unclear. Therefore, additional research focused on the TC of Al–Si is required.

Hasselman reported that the TC of composites is related to the thermal boundary resistance (TBR).[18] The effective medium theory that was derived by Nan considered the interfacial thermal resistance and the size and shape of the reinforcement to predict the TC of composites that were reinforced with a low fraction of microsized particles.[19] However, effective medium theory is not applicable for particles at the nanoscale. Due to increased interface scattering and because the nanoparticle size approaches the phonon mean-free path, TC of the nanoparticle and matrix are not equal to their bulk values. To address this problem, a modified effective medium approximation (EMA)

State Key Laboratory of Solidification Processing, Northwestern Polytechnical University, Xi'an 710072, P.R. China. E-mail: jdp@mail.nwpu.edu.cn; Fax: +86-29-88492642

that considers the increased interfacial scattering and interfacial thermal resistance based on Nan's model was proposed by Minnich and Chen.[20] According to the modified EMA, the interfacial density and TBR affect the TC of the nanocomposite. In addition, Huang *et al.* investigated the effect of the standard deviation (SD) of the nanoparticle size as well as the chemical bonding of the TC of nanocomposites.[21,22] SD can significantly affect the TC of nanocomposites. In addition, thermal boundary resistance can be greatly reduced with an increase in the chemical bonding ratio between two crystal phases.

These models are based on a uniform distribution of nanoparticles in the matrix. At present, several investigations are available on the TC of nanocomposites for graphene and CNT.[23–25] The distribution of reinforcement is uniform in graphene- and CNT-reinforced metal matrix nanocomposites fabricated by solid-state or other processes. Unlike graphene- and CNT-reinforced nanocomposites, during solidification, nanoparticles will redistribute and segregate in the matrix *via* a liquid process. Furthermore, the redistribution of nanoparticles leads to the refinement of microstructures and the modification of microstructures' morphology. Thus, additional research on the effect of nanoparticles on TC is necessary.

To address these issues, we studied Al–17Si–3.5Cu with the addition of 1.0–3.0 wt% SiC nanoparticles (SiC_{nps}) *via* a solidification process combined with ultrasonic treatment. And interfacial nanocomposites layer was proposed to investigate the effect of SiC_{nps} distributed at the interface between Si and Al on TC. The refinement of primary Si with SiC_{nps} addition in Al–Si alloys was studied *via* high-resolution transmission electron microscopy (HRTEM).

2. Experimental procedure

Al–17Si–3.5Cu samples (Fu Metal Material Co., Ltd.) were melted in an alumina crucible by using an electric resistance furnace, and 1.0, 2.0 and 3.0 wt% SiC_{nps} (Shanghai Yao Tian Nano Material Co., Ltd.) were added to the molten Al alloys. The average particle size of the added SiC_{nps} was 30 nm. The apparatus and solidification process combined with ultrasonic treatment that was used to prepare the SiC_{nps}/Al–17Si–3.5Cu materials is shown in detail in ref. 26. The melt was cast by using a cast-iron cylindrical mold that had been preheated to 400 °C. For comparison, Al–17Si–3.5Cu samples without SiC_{nps} addition were prepared by an equivalent process.

Metallographic samples were cut at 51 mm from the bottom of the castings, and then ground with 240-, 600- and 1200-grit emery papers in turn and polished with a 2 μm diamond polishing agent. The samples were etched lightly by using a 0.5% aqueous HF solution. Samples were also etched deeply for 2 h to reveal the three-dimensional morphology of the Si phase. The Si-phase morphology was characterized by using scanning electron microscopy (SEM; FEI Nova NanoSEM 450, Hillsboro, USA) with energy dispersive X-ray spectroscopy (EDS; INCA X-Max, Oxford, UK). X-ray diffraction (XRD; PANalytical X'Pert PRO, Almelo, The Netherlands) was used to analyze the crystalline phases of the Al–17Si–3.5Cu and SiC_{nps}/Al–17Si–3.5Cu. The distributions of SiC_{nps} in the eutectic Al regions and at the interface between Si and Al were investigated using HRTEM with high-angle annular dark-field scanning (HAADF, Tecani F30 G′, FEI, Hillsboro, OR, USA). A laser-flash apparatus (LFA 447, NETZSCH, Selb, Germany) was used to investigate TC of the SiC_{nps}/Al–17Si–3.5Cu samples at room temperature. Results were based on an average of the three samples. To test the TC of the samples, all samples were machined into 3 mm-thick, 12.7 mm-diameter disks. The sample density was determined by the Archimedes method from three repeated measurements, and the specific heat capacity was calculated by the rule of mixtures based on the fraction of each phase. The TC of the samples was the product of the density, thermal diffusivity and specific heat capacity. Image Pro-Plus soft (IPP, Media Cybernetics, Rockville, MD, USA) was applied to measure the average size of primary Si. According to ASTM B108-03a, all samples were cast as tensile bars with a gauge diameter of 5 mm and machined to the specified dimensions according to ASTM E8 with a diameter of 3 mm and a gauge length of 15 mm for the tensile test. A tensile testing machine (INSTRON 3382, INSTRON, Norwood, MA, USA) was used to study the tensile properties of the samples with a crosshead speed of 1 mm min^{-1}. All results were based on the average of three samples.

3. Results

3.1 Effect of SiC_{nps} on the microstructure of SiC_{nps}/Al–17Si–3.5Cu

The XRD patterns that were obtained for Al–17Si–3.5Cu and the 3.0 wt% SiC_{nps}/Al–17Si–3.5Cu samples are shown in Fig. 1(a) and (b), respectively. Fig. 1(a) shows that Al–17Si–3.5Cu is composed of Al, $CuAl_2$ and Si phases only. Fig. 1(b) shows that the SiC_{nps}/Al–17Si–3.5Cu sample includes four crystalline phases, namely, Al, $CuAl_2$, Si and SiC. A comparison of Fig. 1(a) and (b) indicates that SiC_{nps} was incorporated into the Al–17Si–

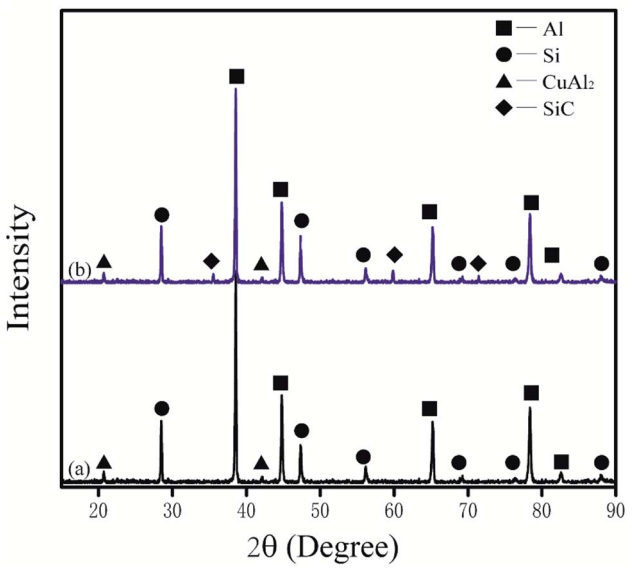

Fig. 1 XRD patterns of Al–17Si–3.5Cu alloy (a) and 3.0 wt% SiC_{nps}/Al–17Si–3.5Cu sample (b).

3.5Cu alloy, and in addition to $CuAl_2$, no other intermetallic crystalline materials were detected. Therefore, the SiC_{nps} did not react visibly with the matrix alloy.

The morphology and size of primary Si in the Al–17Si–3.5Cu with different SiC_{nps} additions are presented in Fig. 2. The microstructures of Al–17Si–3.5Cu were characterized by coarse

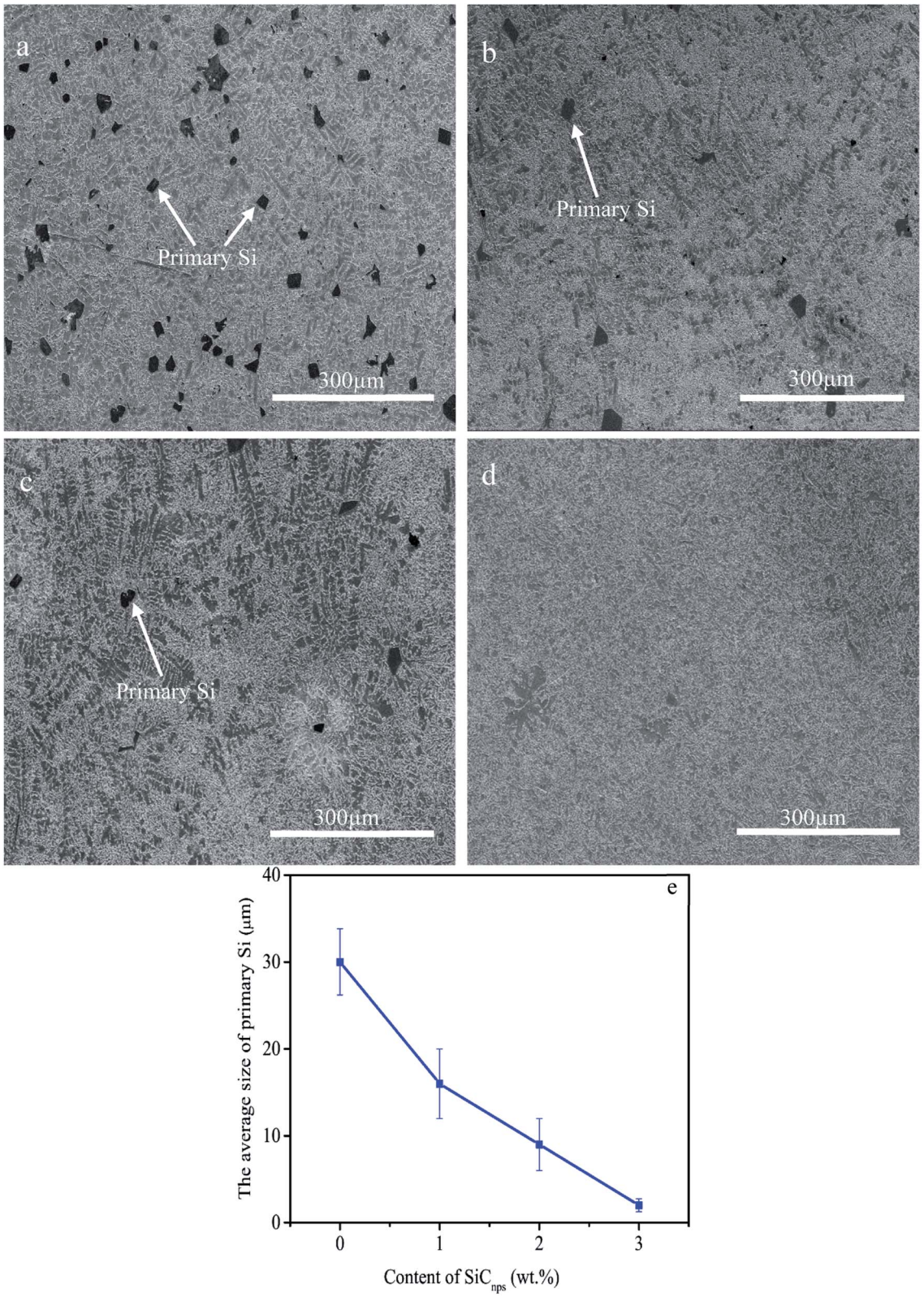

Fig. 2 Morphology of primary Si in Al–17Si–3.5Cu with different SiC_{nps} additions: (a) Al–17Si–3.5Cu, (b) 1 wt% SiC_{nps}/Al–17Si–3.5Cu, (c) 2 wt%/Al–17Si–3.5Cu, (d) 3 wt%/Al–17Si–3.5Cu, and (e) average size of primary Si *vs.* content of SiC_{nps}.

primary Si with an average grain size of 30 μm and eutectic microstructures. Fig. 2(b)–(d) show that with an increase in SiC_{nps} content from 1 wt% to 3 wt%, the primary Si is refined significantly and the coarse primary Si content per unit volume is reduced clearly. When the addition of SiC_{nps} reaches 3 wt%, the coarse primary Si is refined completely. Hence, the addition of SiC_{nps} leads to a refinement of primary Si in the hypereutectic Al–Si alloy. The average size variation of primary Si with the SiC_{nps} content is shown in Fig. 2(e). When the SiC_{nps} content is 1 wt%, the average size of the primary Si is 16 μm, which is reduced by 47% compared with Al–17Si–3.5Cu. The average size of the primary Si with 3 wt% SiC_{nps} addition was reduced to 2 μm, which is a 97% decrease compared with Al–17Si–3.5Cu.

Fig. 3 shows SEM images of the 3.0 wt% SiC_{nps}/Al–17Si–3.5Cu. Fig. 3(a) shows that compared with Al–17Si–3.5Cu, the primary Si and eutectic Si were refined extensively in 3.0 wt% SiC_{nps}/Al–17Si–3.5Cu. The cross-sectional morphology of many Si phases became spheroidized. Because of the nanoparticles, the morphology of some Si phases transformed from platelets to more curved and rounder. Fig. 3(b) shows that the nanoparticles distribute uniformly and are dispersed completely in the eutectic Al. To obtain the nanoparticle composition, EDS spot analysis of the area marked with "+" in Fig. 3(b) was conducted. According to the EDS results, four elements were detected: C, Si, Al and Cu. According to the XRD results, $CuAl_2$ is present in 3.0 wt% SiC_{nps}/Al–17Si–3.5Cu. Hence, the Cu signal

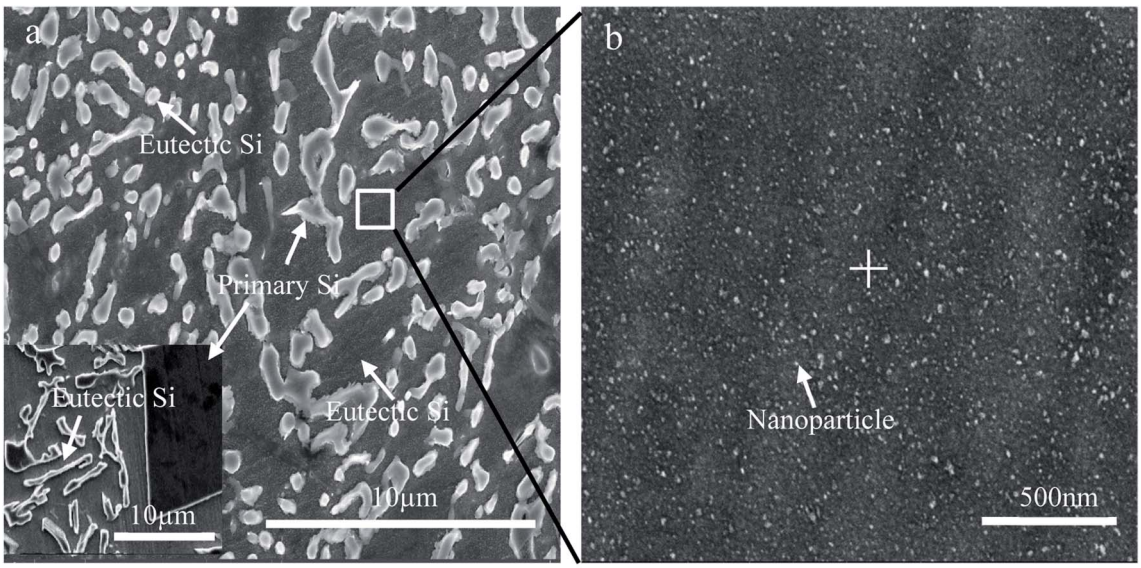

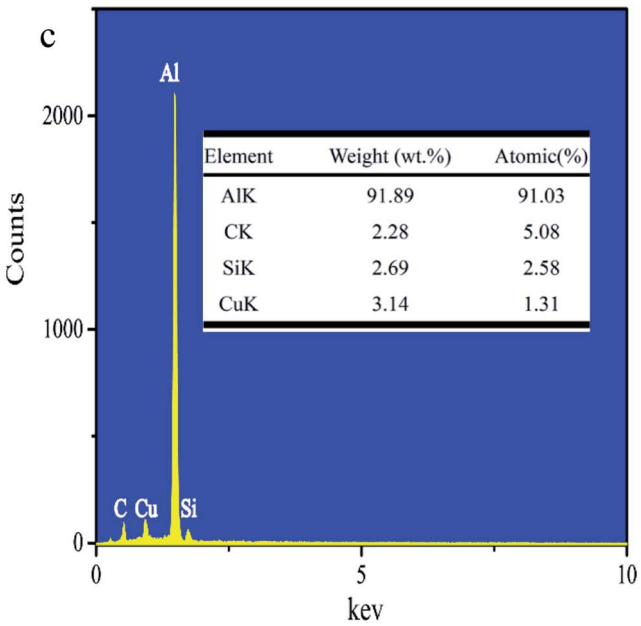

Fig. 3 SEM images of 3.0 wt% SiC_{nps}/Al–17Si–3.5Cu. (a) Morphology of primary Si and eutectic Si in 3.0 wt% SiC_{nps}/Al–17Si–3.5Cu, (b) distribution of nanoparticles in eutectic Al, and (c) EDS spot analysis of the area marked "+" in (b). The inset in (a) shows morphology of primary Si and eutectic Si in Al–17Si–3.5Cu.

comes from $CuAl_2$. Therefore, in addition to $CuAl_2$, SiC_{nps} are present in eutectic Al.

To illustrate the distribution of nanoparticles, microstructures and elemental mapping micrographs for 3.0 wt% SiC_{nps}/Al–17Si–3.5Cu are shown in Fig. 4. Fig. 4(a) shows the SiC_{nps}/Al–17Si–3.5Cu microstructures. Fig. 4(b)–(e) reveal the spatial distributions of C, Al, Si and Cu, respectively. Elemental C that is derived mainly from SiC_{nps} is distributed mainly around the Si phase and on the Si phase surface. The remaining elemental C distributes in the eutectic Al. The elemental Cu is not enriched around the Si phase. This result shows that the refinement of Si phase results because of nanoparticle distribution on the surface of the Si phase.

SEM images of samples that were etched for 2 h are presented in Fig. 5. The three-dimensional morphology of the Si phase in Al–17Si–3.5Cu is characterized by a large thin plate-like eutectic Si and blocky primary Si. No particles adhere to the Si phase surface. Fig. 5(b) shows that some nanoparticles are distributed on the surface of primary Si in 1 wt% SiC_{nps}/Al–17Si–3.5Cu. Fig. 5(b)–(d) show that with an increasing SiC_{nps} content in the Al–17Si–3.5Cu, nanoparticle distribution on the primary Si surface increased. Fig. 5(d) shows that the primary Si is encapsulated by a dense layer of nanoparticles. The inset in Fig. 5(d) shows that nanoparticles on the surface of primary Si are clear, and except for some nanoclusters, the nanoparticles are well dispersed. Fig. 5(e) shows that some nanoparticles

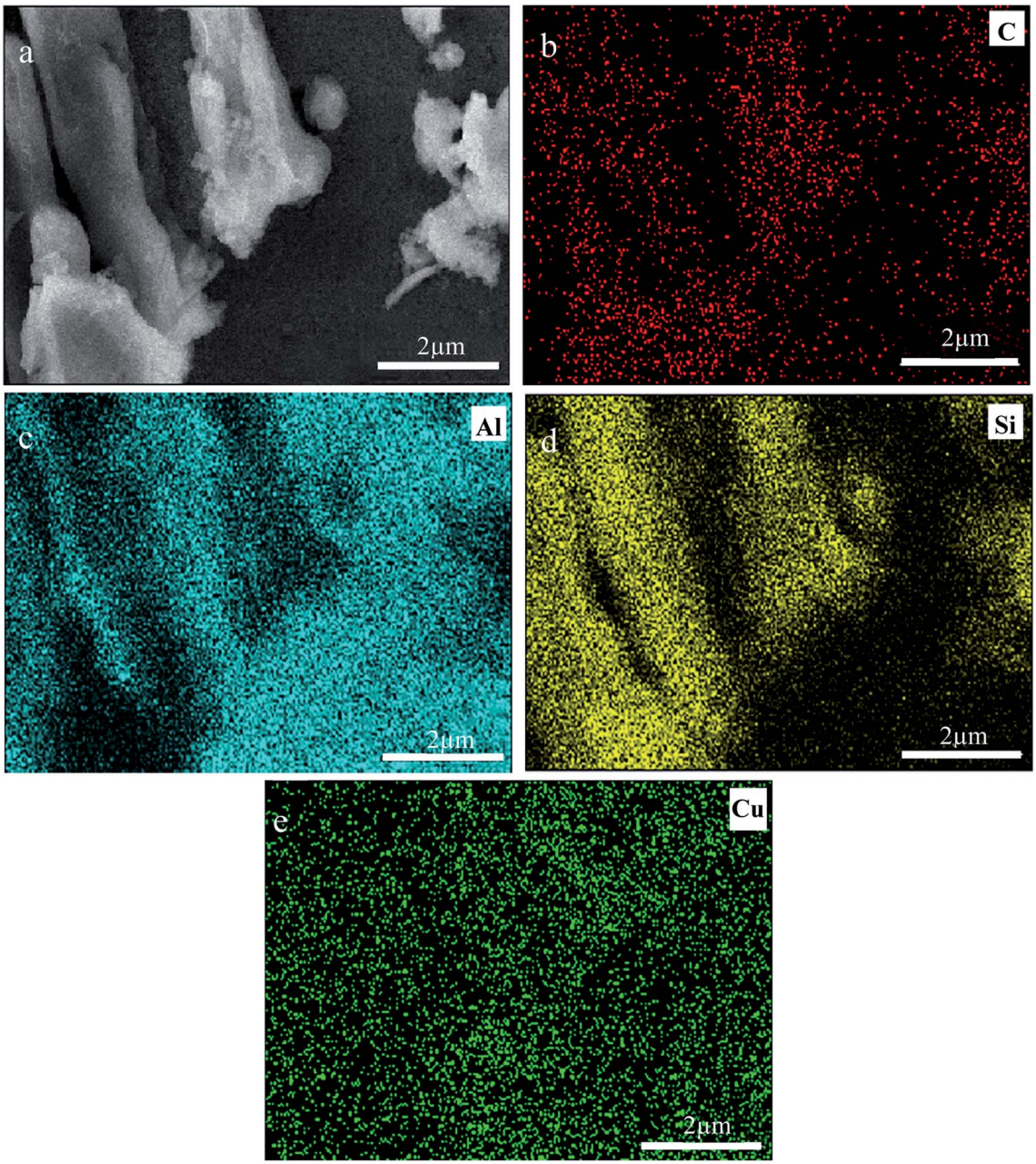

Fig. 4 Microstructures and elemental mapping micrographs of 3.0 wt% SiC_{nps}/Al–17Si–3.5Cu. (a) SEM images, and (b–e) mapping micrographs for elemental C, Al, Si and Cu, respectively.

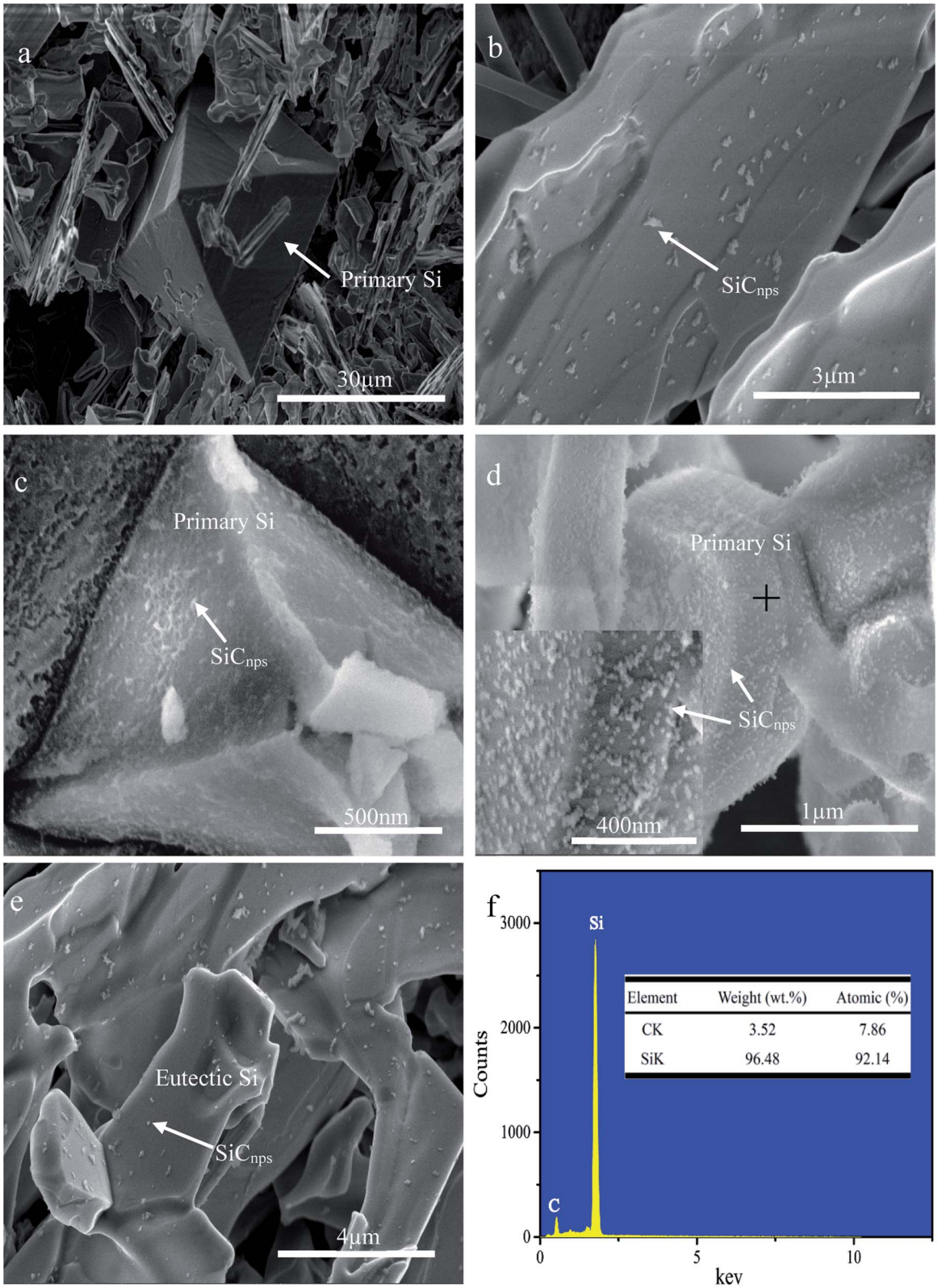

Fig. 5 SEM images of primary Si in Al–17Si–3.5Cu with different SiC_{nps} contents that were etched using a 0.5% HF–water solution for 2 h: (a) Al–17Si–3.5Cu, (b) 1.0 wt% SiC_{nps}/Al–17Si–3.5Cu, (c) 2.0 wt% SiC_{nps}/Al–17Si–3.5Cu, (d) 3.0 wt% SiC_{nps}/Al–17Si–3.5Cu. Inset in (d) is the magnification of the local area on the surface of primary Si, (e) SEM images of eutectic Si in 3.0 wt% SiC_{nps}/Al–17Si–3.5Cu, and (f) EDS analysis of the area marked by "+" in (d).

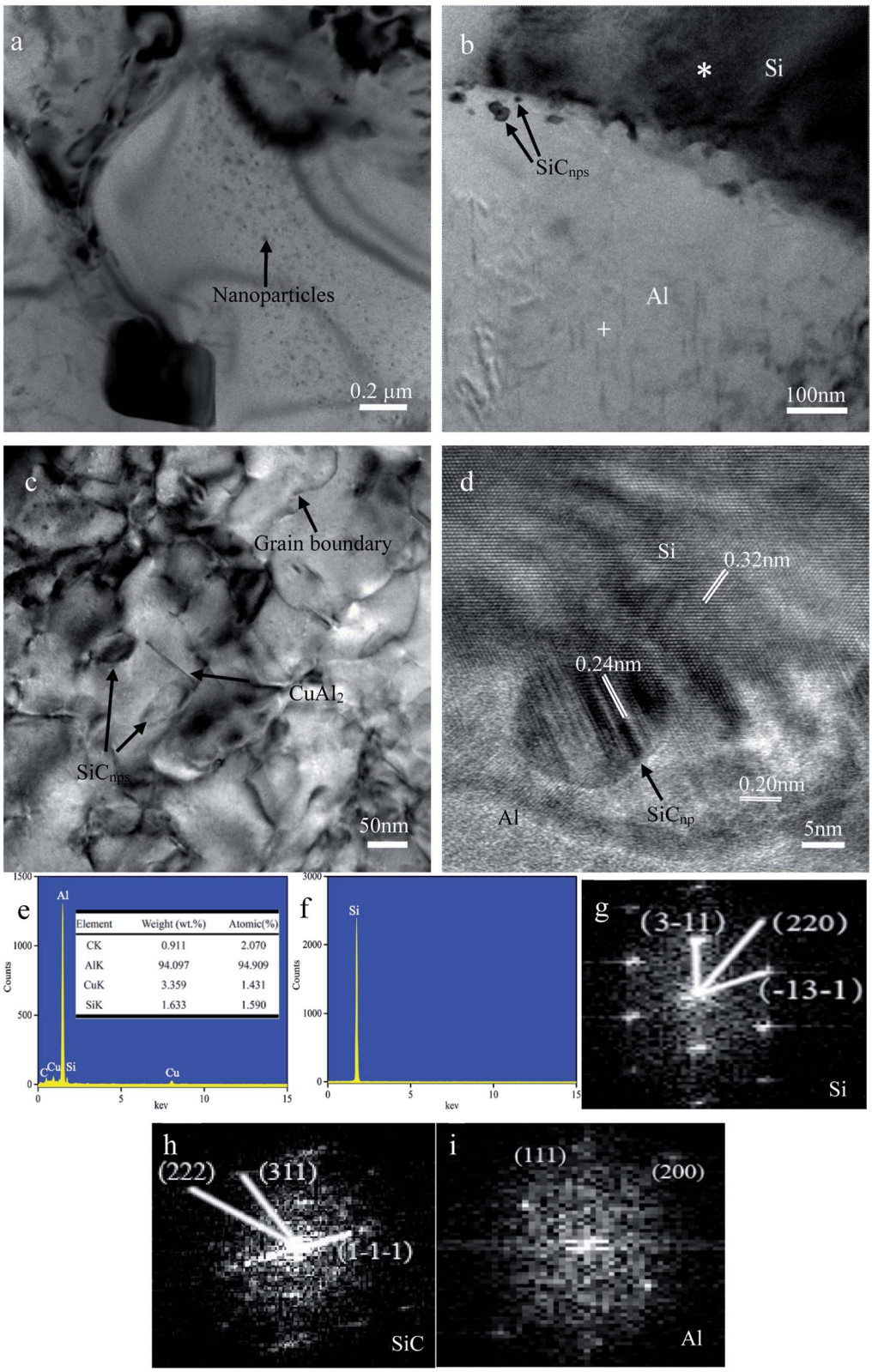

Fig. 6 TEM bright field images of 3.0 wt%SiC_{nps}/Al–17Si–3.5Cu (a) and the interface between Al and primary Si (b), (c) TEM bright field image of the eutectic Al; (d) HRTEM image of the interface between Al and primary Si, (e) and (f) EDS analysis of the area marked by "+" and "*"in (b) respectively, and (g)–(i) are the fast Fourier transformations (FFT) of primary Si, SiC_{np} and Al, respectively.

distribute on the surface of eutectic Si in 3 wt% SiC_{nps}/Al–17Si–3.5Cu. Because of the increase of nanoparticles in alloys, some nanoparticles distribute at the interface between eutectic Si and Al. To obtain the nanoparticle composition, EDS analysis was conducted on the marked area in Fig. 5(d). Fig. 5(f) shows that only elemental Si and C were detected. Therefore, nanoparticles on the primary Si surface are SiC. This result is consistent with the EDS element mapping analysis in Fig. 4.

TEM analysis was used to investigate the effect of SiC_{nps} on the primary Si microstructure. Fig. 6 shows a series of HRTEM images from 3.0 wt% SiC_{nps}/Al–17Si–3.5Cu. Fig. 6(a) shows that many nanoparticles, including $CuAl_2$ and SiC_{nps}, are distributed in the SiC_{nps}/Al–17Si–3.5Cu microstructures. Fig. 6(b) shows that some nanoparticles are distributed at the interface between the primary Si and Al. Nanoparticles at the interface between Si and Al restrict primary Si growth by inhibiting solute atom diffusion.[16] Fig. 6(c) shows that some acicular and granular second phases, namely $CuAl_2$ and SiC_{nps}, respectively, are distributed in the eutectic Al. The nanoparticles are dispersed uniformly. Fig. 6(d) shows a HRTEM image of the interface between the primary Si and Al. SiC_{np} with a 30 nm diameter and an interplanar distance of 0.24 nm distributes at the interface between primary Si with an interplanar distance of 0.32 nm and Al with an interplanar distance of 0.20 nm. Fig. 6 (e) and (f) show EDS analysis of the area marked by "+" and "*" in (b), respectively. From Fig. 6(e), four elements were detected: C, Si, Al and Cu. It indicates that two phases, SiC and $CuAl_2$, exist in eutectic Al. This result is consistent with Fig. 6(b). According to EDS results shown in Fig. 6(f), it can be seen that this phase is the Si phase. Fig. 6 (g)–(i) show the fast Fourier transformation of primary Si, SiC_{np} and Al, respectively. The electron diffraction spot of the phases in Fig. 6 (g)–(i) was consistent with that of Si, SiC_{nps} and Al, respectively. No interfacial product was observed at the interface between the SiC_{np} and Si and Al.

To evaluate the interface between the primary Si and Al, HADDF images of the interface between primary Si and Al are shown in Fig. 7(a). Many nanoparticles are distributed at the interface and acicular phase, and some granular phases exist in the eutectic Al. Fig. 7(b) and (c) show EDS spot analysis of the area marked with "*" and "+" in Fig. 7(a), respectively. EDS results of

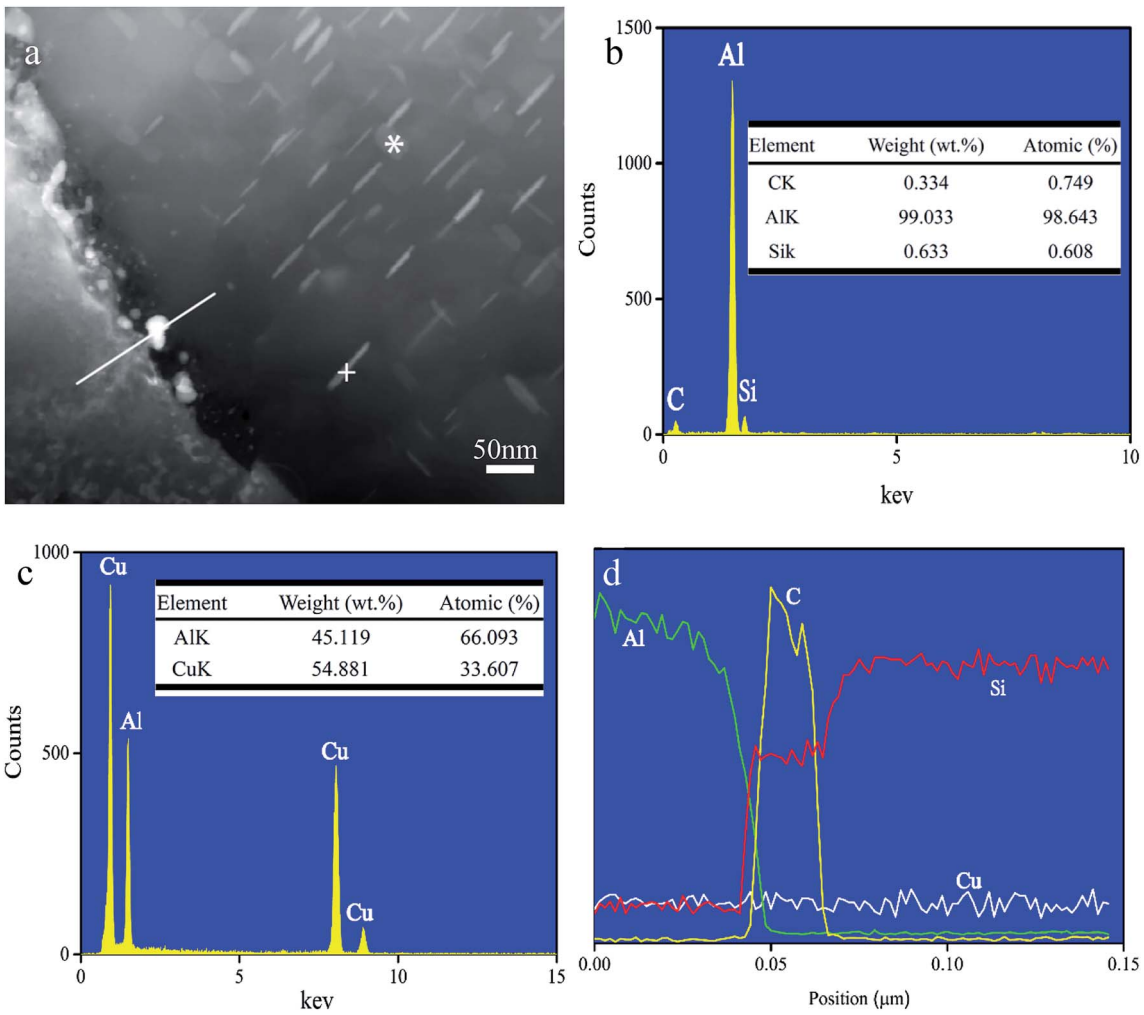

Fig. 7 (a) High-angle annular dark-field (HADDF) images of the interface between primary Si and Al, (b) EDS spot analysis of area marked with "*" in (a); (c) EDS spot analysis of the area marked "+" in (a), and (d) EDS line-scan results of elemental Al, C, Si and Cu along white line in (a).

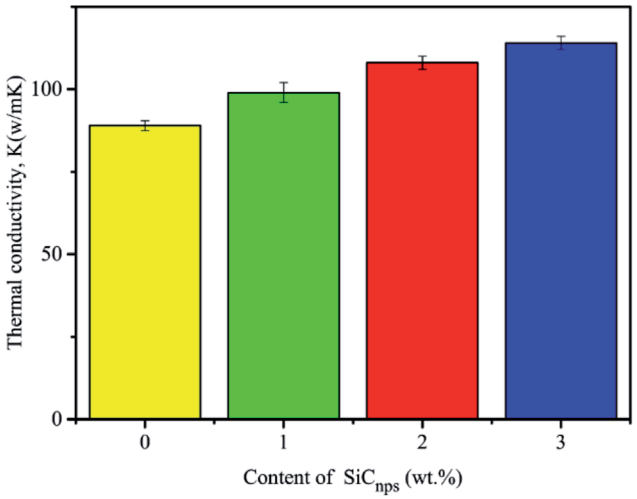

Fig. 8 Thermal conductivity of SiC_{nps}/Al–17Si-3.5Cu and Al–17Si-3.5Cu.

the granular phase show that elemental Al, Si and C are present. In addition to Al, Si and C, the signal derives mainly from SiC_{np}. According to the EDS result in Fig. 7(c), elemental Cu and Al originate from the acicular phase. Combined with XRD analysis, the acicular phase is $CuAl_2$. EDS line-scanning results of the interface between the primary Si and Al are shown in Fig. 7(d). The line-scanning results show that the elements Si and C are enriched at the interface between the primary Si and Al, which indicates that the SiC_{nps} that is distributed at the interface leads to the refinement of primary Si. These results are consistent with the EDS mapping analysis in Fig. 4.

3.2 Effect of SiC_{nps} on TC and tensile strength of SiC_{nps}/Al–17Si–3.5Cu

Fig. 8 shows that the TC of 1 wt% SiC_{nps}/Al–17Si–3.5Cu, 2 wt% SiC_{nps}/Al–17Si–3.5Cu, 3 wt% SiC_{nps}/Al–17Si–3.5Cu and Al–17Si–3.5Cu was 98, 108, 114 and 89 W m^{-1} K^{-1}, respectively. As the content of SiC_{nps} increases, the TC of the SiC_{nps}/Al–17Si–3.5Cu increases. Compared with Al–17Si–3.5Cu, the improvement in TC of the 3 wt% SiC_{nps}/Al–17Si–3.5Cu was 28%, which indicates that the TC of SiC_{nps}/Al–17Si–3.5Cu can be improved by SiC_{nps} addition.

Engineering stress–strain curves and tensile properties of the SiC_{nps}/Al–17Si–3.5Cu and Al–17Si–3.5Cu are shown in Fig. 9. The tensile properties of the SiC_{nps}/Al–17Si–3.5Cu are improved significantly compared with those of the Al–17Si–3.5Cu. The yield strength (YS), ultimate tensile strength (UTS) and elongation (EL) of SiC_{nps}/Al–17Si–3.5Cu increased with the increase

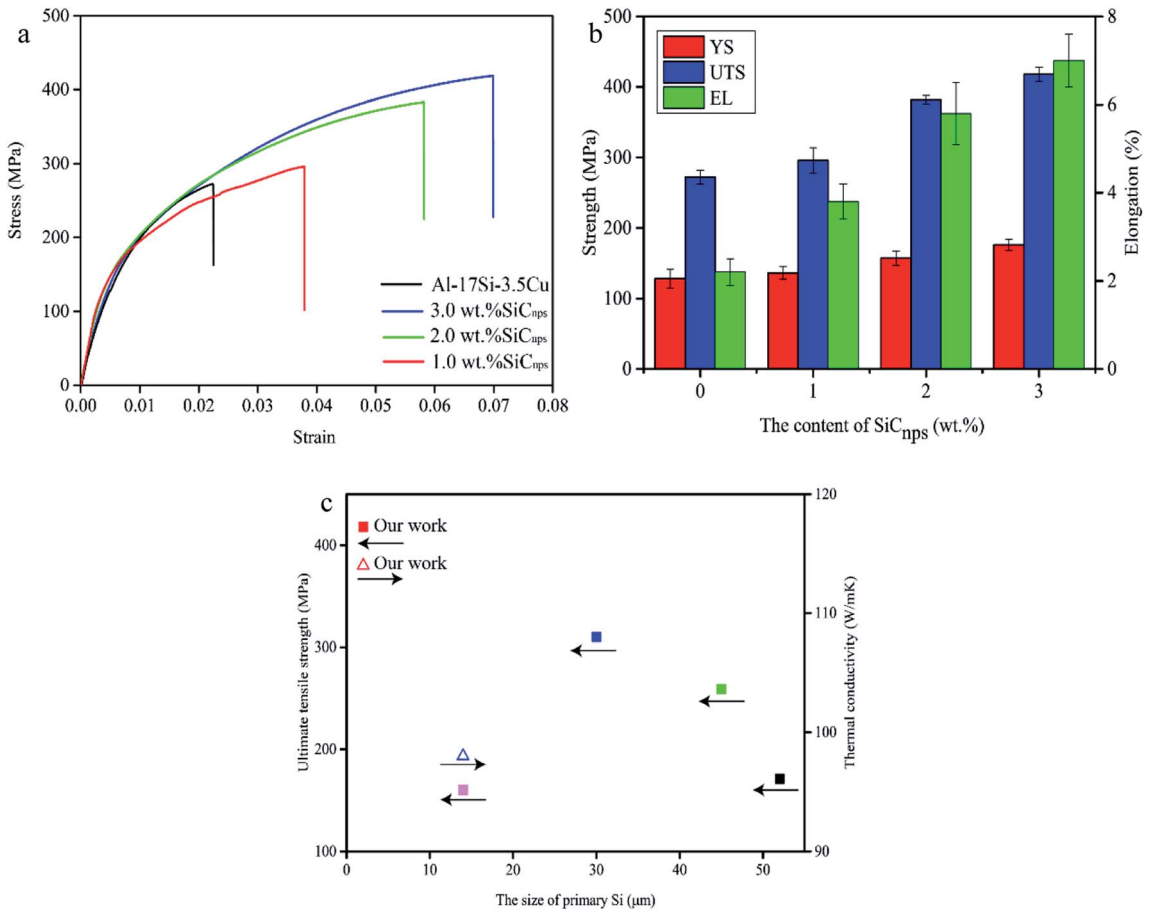

Fig. 9 Engineering stress–strain curves and tensile properties of SiC_{nps}/Al–17Si–3.5Cu and Al–17Si–3.5Cu: (a) engineering stress–strain curves, and (b) UTS, YS and elongation; and (c) comparison of UTS and TC with other reports of hypereutectic Al–Si alloys.[12,27–30]

in SiC_{nps} content. The YS, UTS and EL of 3 wt% SiC_{nps}/Al–17Si–3.5Cu were ~176 MPa, 418 MPa and 7% respectively, which represents an increase of 37.5%, 53.7% and 218% compared with the Al–17Si–3.5Cu, respectively. The primary Si is refined significantly because of SiC_{nps} distribution at the interface between the primary Si and Al, which results in an improvement in the UTS, YS and EL of the SiC_{nps}/Al–17Si–3.5Cu. Furthermore, nanoparticles can inhibit dislocation motion, which leads to the Orowan strengthening effect. Compared with previous work,[12,27–30] the average size of the primary Si in this study is smaller, and the UTS and TC of our samples are higher than those previously reported, as shown in Fig. 9(c).

4. Discussion

4.1 Analyses of thermal properties

The previous analysis indicates that an increase in TC of SiC_{nps}/Al–17Si–3.5Cu occurs because the addition of SiC_{nps} and the distribution of SiC_{nps} at the interface between the primary Si and Al leads to refinement of the primary Si. Therefore, the SiC_{nps} distribution is closely related to TC of the sample. To investigate the effect of SiC_{nps} distribution at the interface between Si and Al on SiC_{nps}/Al–17Si–3.5Cu TC, SiC_{nps} distributed at the interface between Si and Al were assumed to be a SiC_{nps}/Al nanocomposite layer. Fig. 10 shows that compared with the Al/Si interface in Al–17Si–3.5Cu, hypothetical interfacial nanocomposite layers were added to the Al/Si interface in SiC_{nps}/Al–17Si–3.5Cu.

To simplify the analysis, Si phases, including primary Si, eutectic Si and SiC_{nps}, are regarded as spheres. $CuAl_2$ and Al are regarded as a whole, that is, a matrix phase.

Interfacial scattering needs to be considered in nanocomposites in which the characteristic nanoparticle length is of the order of or smaller than the phonon mean free path (MFP). Because of boundary scattering of the energy carriers in the nanoparticles with the nanoparticle surface, the TC k_p of the nanoparticles is given by:[31]

$$k_p = \frac{K_p}{1 + l_p/r} \tag{1}$$

where K_p is the bulk TC of the nanoparticles, l_p is the MFP of the energy carriers in the nanoparticles and r is the nanoparticle radius.

We consider the scattering of energy carriers in the matrix with the nanoparticle surface, and the TC k_m of the matrix is as follows:[31]

$$k_m = \frac{K_m}{1 + l_m \sigma_* f} \tag{2}$$

where K_m is the bulk TC of the matrix, l_m is the MFP of the energy carriers in the matrix, f is the content of nanoparticles in the nanocomposites and σ_* is the collision cross-section per unit volume of the nanoparticles. For spherical particles:

$$\sigma_* = \frac{3}{4r} \tag{3}$$

By replacing k_p and k_m in Nan's model with their corresponding modified values, given by eqn (1) and (2), the TC K of the matrix, considering of interfacial scattering and interfacial thermal resistance, is determined by:

$$\frac{K}{k_m} = \frac{k_p(1+2\alpha) + 2k_m + 2f\left[k_p(1-\alpha) - k_m\right]}{k_p(1+2\alpha) + 2k_m - f\left[k_p(1-\alpha) - k_m\right]} \tag{4}$$

Compared with Al–17Si–3.5Cu, after SiC_{nps} addition, the TC increment Δk^* of the matrix phase is given by:

$$\Delta k^* = \frac{f_m\left[k_p(1-\alpha) - k_m\right]}{k_p(1+2\alpha) + 2k_m - f_m\left[k_p(1-\alpha) - k_m\right]} \tag{5}$$

where f_m is the SiC_{nps} content in the matrix and α is a dimensionless parameter that is determined from:

$$\alpha^{-1} = k_m/k_p + a_k/r \tag{6}$$

where $a_k = R_{Bd}k_m$, called the Kapitza radius, and R_{Bd} is the interfacial thermal resistance (*i.e.*, 6.85×10^{-9} m^2 K W^{-1} for SiC and Al).[32]

However, due to the concentration of nanoparticles distributed at the interface being higher than that of nanoparticles in the matrix, the size distribution of the nanoparticles has a great influence on the interfacial nanocomposite layer. Nanoparticle size distribution obeys a log-normal distribution, and ln μ and σ are the mean and standard deviation of the variable's natural logarithm, respectively. Considering the size distribution of the

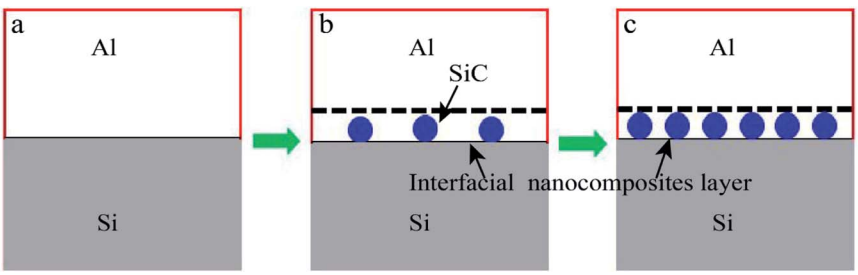

Fig. 10 Schematic diagram of the interface between Si and Al in Al–17Si–3.5Cu and SiC_{nps}/Al–17Si–3.5Cu: (a) the interface between Si and Al in Al–17Si–3.5Cu, (b) the interface between Si and Al in Al–17Si–3.5Cu with adding a small amount of SiC_{nps}, and (c) the interface between Si and Al in Al–17Si–3.5Cu with adding a large amount of SiC_{nps}.

nanoparticles, the average TC of the nanoparticles and the matrix are expressed as follows, respectively:[21]

$$k_p^* = \frac{k_p}{1 + \frac{l_p}{\mu\, e^{5\sigma^2/2}}} \tag{7}$$

$$k_m^* = \frac{k_m}{1 + \frac{3fl_m}{4(1-f)\mu}\exp\left(-\frac{5}{2}\sigma^2\right)} \tag{8}$$

and the TC k_{in}^{eff} of the interfacial nanocomposites layer is determined as:

$$\frac{k_{in}^{eff}}{k_m^*} = \frac{k_p^*(1+2\alpha) + 2k_m^* + 2f\left[k_p^*(1-\alpha) - k_m^*\right]}{k_p^*(1+2\alpha) + 2k_m^* - f\left[k_p^*(1-\alpha) - k_m^*\right]} \tag{9}$$

Furthermore, to simplify the calculation, the SD of a log-normal distribution is as follows:

$$SD = \mu\, e^{\sigma^2/2}\sqrt{e^{\sigma^2} - 1} \tag{10}$$

The total interfacial thermal resistance R between Al and Si in SiC_{nps}/Al–17Si–3.5Cu is expressed as:

$$R = R_{Si-in} + R_{Al-in} + R_{in} \tag{11}$$

where R_{Si-in} is the interfacial thermal resistance between Si and the interfacial nanocomposite layer, R_{Al-in} is the interfacial thermal resistance between Al and the interfacial nanocomposite layer, and R_{in} is the thermal resistance of the interfacial nanocomposite layer:

$$R_{in} = \frac{2r}{k_{in}^{eff}} \tag{12}$$

We assume that the relationship for diffuse scattering of the interfacial thermal resistance R from Chen[33] can be used:

$$R \approx 4\left(\frac{C_1 v_1 + C_2 v_2}{C_1 v_1 C_2 v_2}\right) \tag{13}$$

where v and C are the phonon group velocity and the volumetric specific heat respectively.

The specific heat C_{in} of the interfacial nanocomposites layers is defined as:[31]

$$C_{in} = (1-f)C_{Al} + fC_{SiC} \tag{14}$$

The combined phonon group velocity v_{in} of the interfacial nanocomposites layers is determined as:[34]

$$\frac{1}{v_{in}} = \frac{1}{3v_{Al}}\sqrt{\frac{\rho_{in}}{\rho_{Al}}}\left(\sqrt{1 - \frac{E_{Al} - E_{SiC}}{E_{SiC}}f} + 2\sqrt{1 - \frac{G_{Al} - G_{SiC}}{G_{SiC}}f}\right) \tag{15}$$

where v_{Al} is the phonon group velocity of Al; E_{SiC}, G_{SiC} and E_{Al}, G_{Al} are the Young's modulus and shear modulus of Al and SiC, respectively; ρ_{Al} and ρ_{SiC} are the density of Al and SiC (*i.e.*, 2.7 and 3.2 g cm^{-3}) and $\rho_{in} = (1-f)\rho_{Al} + f\rho_{SiC}$.

The effective TC k_{Si}^{eff} of Si is expressed as:

$$k_{Si}^{eff} = \frac{k_{Si}}{1 + \frac{2Rk_{Si}}{d}} \tag{16}$$

where k_{Si} is the TC of Si, R is the thermal resistance and d is the Si size. The validity of eqn (16) for calculating the effective TC of irregular inclusions, such as graphite, has been confirmed previously.[35]

The thermal resistance R between Al and Si in Al–17Si–3.5Cu is given by:

$$R_{Al-Si} = 4\left(\frac{C_{Al}v_{Al} + C_{Si}v_{Si}}{C_{Al}v_{Al}C_{Si}v_{Si}}\right) \tag{17}$$

Fig. 11 shows the effective TC of Si based on the parameters in Table 1 for SiC_{nps}/Al–17Si–3.5Cu. Fig. 11(a) shows that compared with the effective TC of Si in Al–17Si–3.5Cu, the effective TC of Si is improved with a SiC_{nps} addition, especially when the content of SiC_{nps} is within a certain range (*i.e.* 0–0.5 for SD = 10); the Si size and SD have a significant effect on the effective TC of the Si. Fig. 11(b) shows that the interfacial thermal resistance between Si and Al increases with an increase in nanoparticle content at the interface between Si and Al, and decreases with an increase in SD in SiC_{nps}/Al–17Si–3.5Cu. The rate of increase for the interfacial thermal resistance with SiC_{nps} content in a certain range (*i.e.* 0–0.4 for SD = 30) is slow. Due to the small number of nanoparticles added, the number of nanoparticles at the interface is not very high. Hence, the number of nanoparticles at the interface has little effect on the thermal resistance between Si and Al. Moreover, many studies illustrate that Si can form a strong chemical bond with SiC.[38,39] According to thermal boundary resistance, which decreases with increased bonding,[22] the interfacial thermal resistance between SiC and Si is lower than that between Si and Al. The interfacial bonding between SiC and Al is similar to that between SiC and Si. Hence, the interfacial thermal resistance between Si and Al in SiC_{nps}/Al–17Si–3.5Cu is consistently lower than in Al–17Si–3.5Cu, which indicates that nanoparticles can reduce the interfacial thermal resistance between Si and Al.

The key to analyze the influence of nanoparticles on the TC of SiC_{nps}/Al–17Si–3.5Cu is to analyze the influence of nanoparticles on the TC of primary Si and eutectic Si.

Because nanoparticles lead to a refinement of primary Si, the TC increment Δk of primary Si in SiC_{nps}/Al–17Si–3.5Cu with SiC_{nps} addition is shown as:

$$\Delta k = \frac{k_{Si}}{1 + \frac{2R_{Al-Si}^* k_{Si}}{d}} - \frac{k_{Si}}{1 + \frac{2R_{Al-Si}k_{Si}}{d_0}} \tag{18}$$

where R_{Al-Si}^* and d are the interfacial thermal resistance between the primary Si and Al and the size of primary Si in SiC_{nps}/Al–17Si–3.5Cu, respectively, and R_{Al-Si} and d_0 are the interfacial thermal resistance between the primary Si and Al and the size of primary Si in Al–17Si–3.5Cu, respectively.

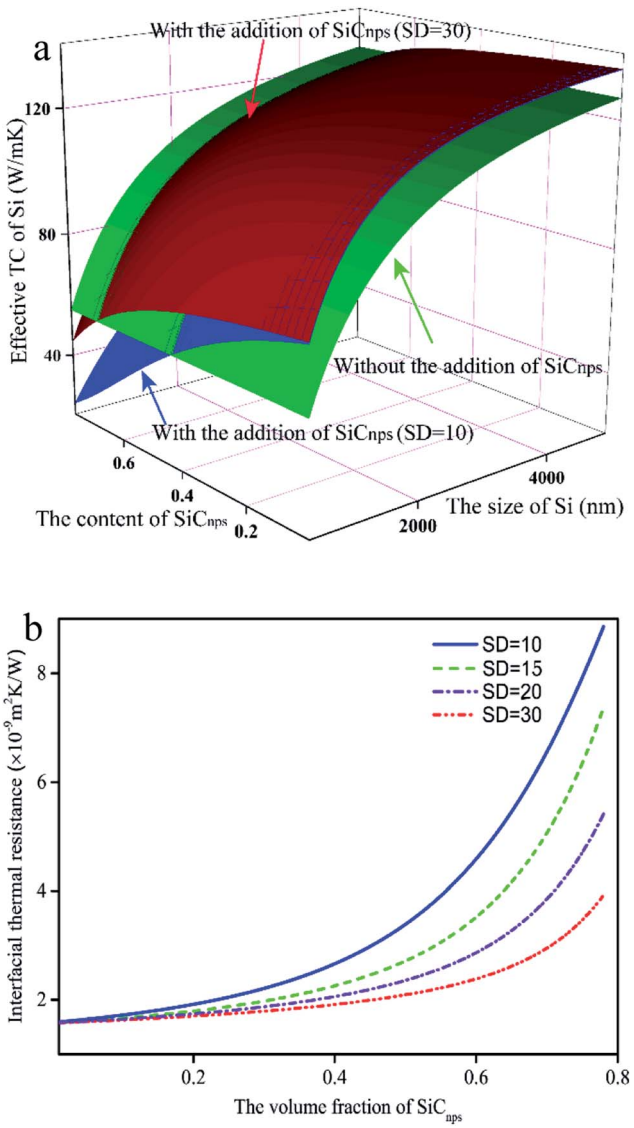

Fig. 11 (a) Effective TC of Si *vs.* the size of Si, the standard deviation (SD) and the content of SiC_{nps}, and (b) the interfacial thermal resistance *vs.* SD and the content of SiC_{nps}.

Because the effect of nanoparticles on the size of eutectic Si is not as significant as that of primary Si, the size of eutectic Si can be considered to be unchanged. The TC increment Δk of eutectic Si in SiC_{nps}/Al–17Si–3.5Cu with the addition of SiC_{nps} is determined by:

$$\Delta k = \frac{2k_{Si}^2\left(R_{Al-Si} - R^*_{Al-Si}\right)D}{\left(D + 2R^*_{Al-Si}k_{Si}\right)\left(D + 2R_{Al-Si}k_{Si}\right)} \quad (19)$$

where D is the size of eutectic Si.

Fig. 12 shows the TC increment of primary Si, eutectic Si and the matrix in SiC_{nps}/Al–17Si–3.5Cu. Fig. 12(a) shows that the effective TC of primary Si decreases with SiC_{nps} addition, but is reduced less with an increase in SD. The increasing content of nanoparticles lead to an increase in the number of nanoparticles at the interface between the primary Si and Al, which in turn refined the primary Si. The refinement of primary Si and the high content of nanoparticles at the interface between primary Si and Al lead to the increase in interfacial thermal resistance. When the content of nanoparticles is high, the SD has a significant effect on the effective TC of the primary Si. The increase in SD leads to less of a reduction in the effective TC of primary Si. Therefore, compared with that of Al–17Si–3.5Cu, the effective TC of primary Si decreased. Fig. 12(b) shows that compared with Al–17Si–3.5Cu, the effective TC of the eutectic Si increased in SiC_{nps}/Al–17Si–3.5Cu. Because fewer nanoparticles were present on the surface of eutectic Si compared with those on the surface of primary Si, the effect of nanoparticles on the size of the eutectic Si was less significant compared with the primary Si. Furthermore, compared with Al–17Si–3.5Cu, because of a small number of nanoparticles on the surface of eutectic Si, the interfacial thermal resistance between Al and eutectic Si was reduced considerably. When the size of the eutectic Si was smaller and the SD was large, the increase in the effective TC of the eutectic Si, which was caused by the nanoparticles, was more significant. Thus, the effective TC of the eutectic Si was improved with the SiC_{nps} addition. Fig. 12(c) shows that the TC of the matrix decreases with an increase in SiC_{nps} content. When 3 wt% nanoparticles were added to the alloys, the content of nanoparticles in the matrix was less than 3%, because a large number of nanoparticles were distributed at the Si/Al interface. Therefore, compared with that of the matrix in Al–17Si–3.5Cu, the TC of the matrix in 3 wt% SiC_{nps}/Al–17Si–3.5Cu decreased by less than 3%. Because a small number of nanoparticles were added to the alloys, nanoparticles caused a limited decrease in the matrix TC. In addition, the above analysis shows that the TC of the alloys will decrease significantly when a large number of nanoparticles are added.

The improvement in the TC of SiC_{nps}/Al–17Si–3.5Cu resulted mainly from the eutectic Si. Compared with Al–17Si–3.5Cu, nanoparticles led to a decrease in the effective TC of primary Si and the matrix in SiC_{nps}/Al–17Si–3.5Cu. However, due to the small interfacial thermal resistance between the eutectic Si and Al, the effective TC of the eutectic Si increased significantly.

Table 1 Material parameters for theoretical calculations[35–37]

Materials	TC (w m^{-1} K^{-1})	Density (g cm^{-3})	Specific heat (J g^{-1} K^{-1})	Phonon velocity (m s^{-1})	Young's moduli (GPa)	Shear moduli (GPa)
Al	237	2.7	0.895	3595	68	26
SiC	248	3.21	0.29	11 600	448	192
Si	148	2.33	0.7	5860	—	—

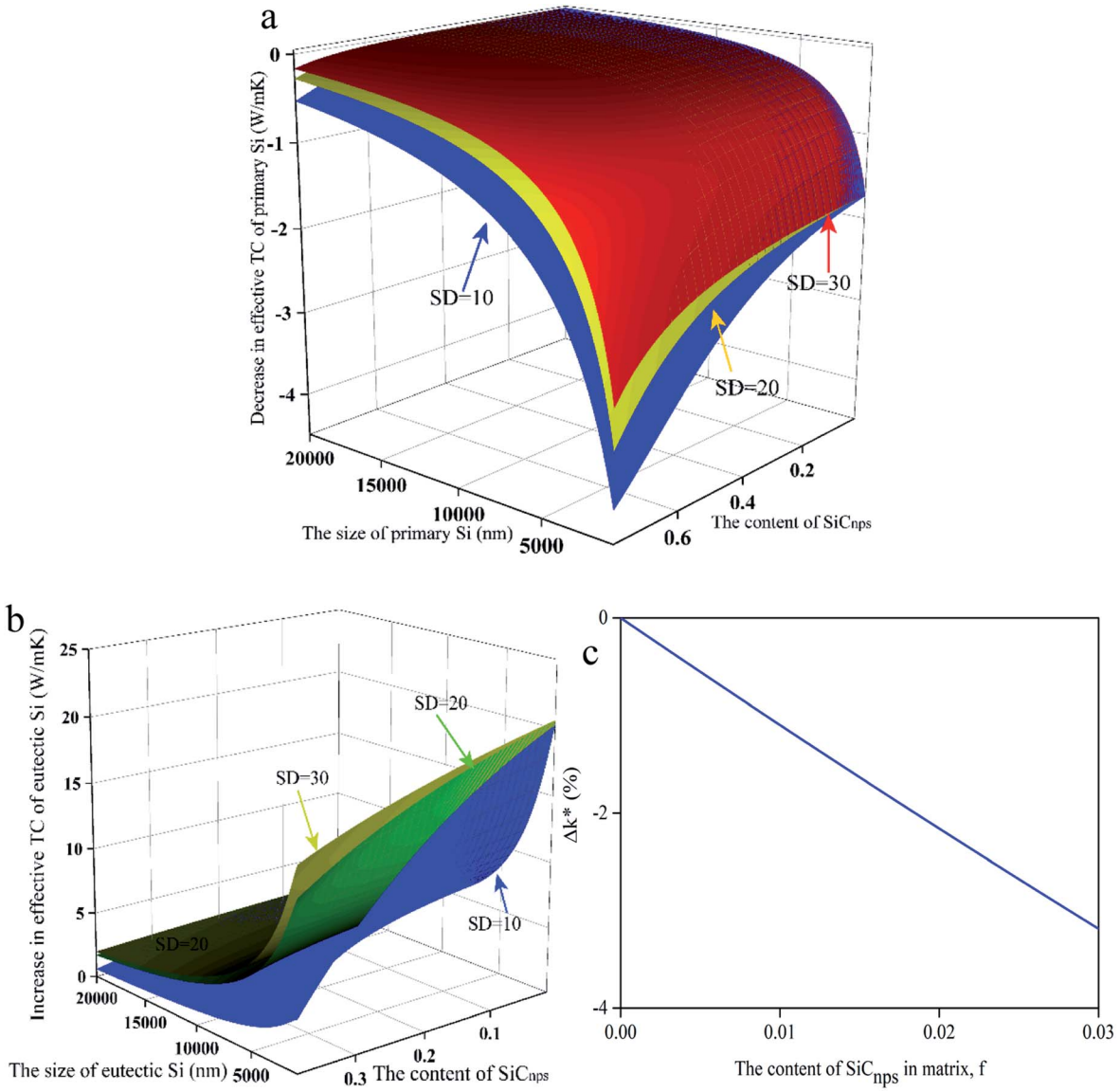

Fig. 12 Compared with Al–17Si–3.5Cu, TC increment of primary Si (a), eutectic Si (b) and the matrix (c) in SiC_{nps}/Al–17Si–3.5Cu respectively.

4.2 Analyses of tensile properties

The significant improvement of YS, UTS and EL of SiC_{nps}/Al–17Si–3.5Cu compared with Al–17Si–3.5Cu resulted because of: (i) the refinement of primary Si. Nanoparticles at the interface between primary Si and Al restrict the growth of the primary Si, which leads to a refinement of primary Si.[2] Numerous investigations have illustrated that crack initiation originates easily from primary Si and eutectic Si.[12,30] Furthermore, cracks may originate from and propagate along the interface between the primary Si and Al. The refinement of primary Si can reduce or eliminate premature crack initiation and fracture. The quantitative relationship of the intrinsic fracture stress (σ_f) on the primary Si is given by Griffith:[30]

$$\sigma_f = \left(\frac{2E\gamma}{\pi C}\right)^{\frac{1}{2}} \quad (20)$$

where E is the Young's modules of the particles, γ is the fracture surface energy and C is the internal defect length. Because of its shorter internal defects compared with that in the coarse primary Si, the fracture stress of the refined primary Si is larger. In addition, the coarse primary Si tends to cause a stress concentration and then crack initiation. Hence, the refinement of primary Si can improve the tensile strength of SiC_{nps}/Al–17Si–3.5Cu. (ii) Orowan strengthening effect. In addition to nanoparticle distribution at the interface between Si and Al, some nanoparticles were distributed uniformly in the eutectic Al. Nanoparticles can hinder the motion of dislocation and pine dislocations and enhance the tensile strength of SiC_{nps}/Al–17Si–3.5Cu. Furthermore, the load transfer between the Al and nanoparticles provides a strengthening effect during the tensile process.

5. Conclusions

SiC_{nps}/Al–17Si–3.5Cu, in conjunction with an addition of 1 wt%, 2 wt% and 3 wt% SiC_{nps}, was prepared in this study, and the effect of SiC_{nps} on the microstructures, TC and tensile properties of SiC_{nps}/Al–17Si–3.5Cu was investigated.

SiC_{nps} addition leads to the refinement of primary Si. When SiC_{nps} is 3 wt%, the primary Si is refined significantly. Nanoparticles at the interface between the Si and Al hinder the growth of the primary Si, which leads to the refinement of primary Si.

The TC of SiC_{nps}/Al–17Si–3.5Cu increases with an increase in SiC_{nps} content. Nanoparticles can reduce the interfacial thermal resistance between Si and Al and increase the effective TC of the Si. The improvement in the TC of SiC_{nps}/Al–17Si–3.5Cu results mainly from eutectic Si.

The YS, UTS and EL of SiC_{nps}/Al–17Si–3.5Cu increase with an increase in SiC_{nps} content. When the SiC_{nps} content is 3 wt%, the YS, UTS and EL of SiC_{nps}/Al–17Si–3.5Cu are ~176 MPa, 418 MPa, and 7%, respectively. Because of the refinement of the primary Si, the tensile strength of SiC_{nps}/Al–17Si–3.5Cu is improved significantly.

Data availability

The raw data required to reproduce these findings are available to download from DOI: 10.17632/xgmh9x8yp8.2.

Conflicts of interest

There are no conflicts to declare.

Acknowledgements

This research did not receive any specific grant from funding agencies in the public, commercial or not-for-profit sectors.

References

1 J. C. Jie, Q. C. Zou, J. L. Sun, Y. P. Lu and T. J. Li, *Acta Mater.*, 2014, **72**, 57–66.
2 D. P. Jiang and J. K. Yu, *J. Mater. Res. Technol.*, 2019, **8**, 2930–2943.
3 C. Xue and J. K. Yu, *Mater. Des.*, 2014, **53**, 74–78.
4 G. R. Li and L. S. Wang, *Appl. Surf. Sci.*, 2019, **483**, 472–480.
5 H. Qiao, X. Z. Zhu, T. Gao, Y. Y. Wu and X. F. Liu, *J. Mater. Sci. Technol.*, 2015, **31**, 391–396.
6 T. Gu, Y. Pan, T. Lu, C. Li and J. Pi, *Mater. Charact.*, 2018, **141**, 115–119.
7 J. G. Jung, T. Y. Ahn, Y. H. Cho, S. H. Kim and J. M. Lee, *Acta Mater.*, 2018, **144**, 31–40.
8 M. Zuo, D. Zhao, X. Teng, H. Geng and Z. Zhang, *Mater. Des.*, 2013, **47**, 857–864.
9 T. Gao, X. Zhu, H. Qiao and X. F. Liu, *J. Alloys Compd.*, 2014, **607**, 11–15.
10 J. Nie, Y. Zhao, Y. Li and F. Wang, *J. Alloys Compd.*, 2019, **777**, 8–17.
11 J. Xiong, H. Yan, S. Zhong and M. Bi, *Metals*, 2019, **9**, 108.
12 Q. Li, T. Xia, Y. Lan, P. F. Li and L. Fan, *Mater. Sci. Eng., A*, 2013, **588**, 97–102.
13 X. Chen, Y. Zhong, T. Zheng, Z. Shen, J. Wang, L. Fan, Y. Zhai, M. Peng, B. Zhou, W. Ren, Z. Lei, Z. Ren and Q. He, *J. Alloys Compd.*, 2017, **714**, 39–46.
14 J. Sun, L. Zhang, G. Wu, W. Liu, Z. Hu and A. Chen, *J. Mater. Process. Technol.*, 2015, **225**, 485–491.
15 H. Choi, H. Konishi and X. Li, *Mater. Sci. Eng., A*, 2012, **541**, 159–165.
16 K. Wang, H. Y. Jiang, Y. X. Wang, Q. D. Wang, B. Ye and W. J. Bing, *Mater. Des.*, 2016, **95**, 545–554.
17 K. Hu, X. Ma, T. Gao, Q. F. Xu, Z. Qian, Y. Wu and X. F. Liu, *J. Alloys Compd.*, 2018, **765**, 113–120.
18 D. P. H. Hasselman and L. F. Johnson, *J. Compos. Mater.*, 1987, **21**, 508–515.
19 C. W. Nan, R. Birringer, D. R. Clarke and H. Gleiter, *J. Appl. Phys.*, 1997, **81**, 6692–6699.
20 A. Minnich and G. Chen, *Appl. Phys. Lett.*, 2007, **91**, 073105.
21 C. L. Huang, X. Qian and R. G. Yang, *Europhys. Lett.*, 2017, **117**, 24001.
22 Z. Huang, C. L. Huang, D. X. Wu and Z. H. Rao, *Comput. Mater. Sci.*, 2018, **149**, 316–323.
23 X. Gao, H. Yue, E. Guo, H. Zhang, X. Lin, L. Yao and B. Wang, *Powder Technol.*, 2016, **301**, 601–607.
24 K. Chu, X. Wang, F. Wang, Y. Li, D. Huang, H. Li, W. Ma, F. Liu and H. Zhang, *Carbon*, 2018, **127**, 102–112.
25 A. Miranda, N. Barekar and B. J. McKay, *J. Alloys Compd.*, 2019, **774**, 820–840.
26 D. P. Jiang and J. K. Yu, *Metals*, 2018, **8**, 572.
27 H. Choi and X. Li, *J. Mater. Sci.*, 2012, **47**, 3096–3102.
28 P. J. Ward, H. V. Atkinson, P. R. G. Anderson, L. G. Elias, B. Garcia, L. Kahlen and J.-M. Rodriguez-ibabe, *Acta Mater.*, 1996, **44**, 1717–1727.
29 K. Y. Sastry, L. Froyen, J. Vleugels, E. H. Bentefour and C. Glorieux, *Int. J. Thermophys.*, 2004, **25**, 1611–1622.
30 C. L. Xu, H. Y. Wang, Y. F. Yang and Q. C. Jiang, *Mater. Sci. Eng., A*, 2007, **452**, 341–346.
31 J. Ordonez-Miranda, R. G. Yang and J. J. Alvarado-Gil, *Appl. Phys. Lett.*, 2011, **98**, 233111.
32 Y. Liu, Y. Dan, Y. Bian and Z. Han, *J. Alloys Compd.*, 2019, **801**, 136–141.
33 G. Chen, *Phys. Rev. B*, 1998, **57**, 14958–14973.
34 S. J. Poon and K. Limtragool, *J. Appl. Phys.*, 2011, **110**, 114306.
35 C. Wang, H. Bai, C. Xue, X. Tong, Y. Zhu and N. Jiang, *RSC Adv.*, 2016, **6**, 107483–107490.
36 W. R. L. Lambrecht, B. Segall, M. Methfessel and M. van Schilfgaarde, *Phys. Rev. B*, 1991, **44**, 3685–3694.
37 S. Tamura, Y. Tanaka and H. J. Maris, *Phys. Rev. B*, 1999, **60**, 2627–2630.
38 X. S. Cong, P. Shen, Y. Wang and Q. C. Jiang, *Appl. Surf. Sci.*, 2014, **317**, 140–146.
39 G. W. Liu, M. L. Muolo, F. Valenza and A. Passerone, *Ceram. Int.*, 2010, **36**, 1177–1188.